

Modeling frequency shifts of collective bubble resonances with the boundary element method

Rudyard Jerez Boudesseul* Elwin van 't Wout*

September 2, 2022

Abstract

Increasing the number of closely-packed air bubbles immersed in water changes the frequency of the Minnaert resonance. The collective interactions between bubbles in a small ensemble are primarily in the same phase, causing them to radiate an axially symmetric field that peaks at a frequency lower than the Minnaert resonance for a single bubble. Differently, large periodic arrays include bubbles that are further apart than half the wavelength so that collective resonances have bubbles oscillating in opposite phases, ultimately creating a fundamental resonance at a frequency higher than the single-bubble Minnaert resonance. This paper explains the transition in resonance behavior through a modal analysis of a mass-spring system and a boundary element method. We significantly reduce the computational complexity of the full-wave solver to a linear dependence on the number of bubbles in a rectangular array. The simulated acoustic fields confirm the initial downshift in resonance frequency and the strong influence of collective resonances when the array has hundreds of bubbles covering more than half the wavelength. These results are essential in understanding the low-frequency resonance characteristics of bubble ensembles, which have important applications in diverse fields such as underwater acoustics, quantum physics, and metamaterial design.

1 Introduction

Gas-filled bubbles immersed in a fluid exhibit interesting dynamics when excited by acoustic pressure fields. For example, the resonance behavior of bubbles at low frequency causes a strong, axially-symmetric scattered field, which has been known since the early work of Minnaert [1] and well studied with analytical expressions [2]. The acoustic interactions between multiple bubbles create different resonances, with a monopole resonance at a lower frequency and sharp superresonances at higher frequencies than the Minnaert resonance [3]. These resonance

*Institute for Mathematical and Computational Engineering, School of Engineering and Faculty of Mathematics, Pontificia Universidad Católica de Chile, Santiago, Chile.
Contact: e.wout@uc.cl

phenomena of bubble ensembles are known as collective resonances [4] or proximity resonances [5] and play an important role in diverse fields such as underwater acoustics [6], metamaterial design [7], and quantum physics [8]. They have been detected in field [9, 10, 11] and laboratory [12, 13, 14, 15, 16, 17, 18] experiments, and studied by a variety of mathematical approaches such as homogenization into effective media [19], modal analysis of ordinary differential equations for mass-spring systems [20], linearized Rayleigh-Plesset equations [21], and numerical methods for the Helmholtz equation [22].

The Minnaert resonance of a single air-filled bubble immersed in water at atmospheric pressure has a frequency of $ka \approx 0.014$, for k the wavenumber and a the bubble's radius, meaning that the bubble is hundreds of times smaller than the wavelength. The interaction between two closely separated bubbles, or a bubble close to a wall, causes a symmetric resonance where both bubbles oscillate in phase and an antisymmetric superresonance with oscillations in opposite phases. The primary resonance is at a lower frequency, whereas the superresonance has a sharp peak at a frequency up to two times the resonance frequency for a single bubble [22]. These characteristics extend to small bubble ensembles, where the dominant resonance displays a downward frequency shift, and several sharp superresonances occur at higher frequencies [3]. Experiments of millimeter-sized air-filled bubbles in water tanks confirm this behavior for cloud [23] and chain [24, 25] configurations, bubbles close to a wall [26, 27], and bubbles in yield-stress fluids [28].

Differently, periodic arrays of bubbles show a dominant resonance at a frequency higher than the Minnaert resonance, as observed in laboratory experiments with bubble metascreens [29, 30] and bubble arrays in yield-stress fluids [31, 32]. These experimental results match well with mathematical models based on monopole resonances of mass-spring systems [31], effective media [33], and finite element methods [34, 32] for infinite periodic arrays. The dynamics of these large bubble arrays exhibit exciting features for metamaterial design such as superabsorption [29], subwavelength focusing [35], and phononic band gaps [36]. The opposite frequency shift of the fundamental resonance for periodic arrays compared to small bubble ensembles is likely caused by bubbles interacting at distances of more than half a wavelength apart, thus influencing other bubbles in opposite phase [32].

This manuscript studies the transition zone between small ensembles and infinite arrays. We use computational methods for structured collections of hundreds of bubbles interacting close to the Minnaert resonance. First, we investigate the collective resonances with a modal analysis of the mass-spring system for monopole point scatterers. Increasing the number of bubbles shows the fundamental resonance decreasing in frequency but then returning and accumulating at a frequency higher than for a single bubble. Furthermore, the incident plane wave field excites other collective resonances that oscillate at a lower frequency than the monopole resonance. Second, we calculate the acoustic field by solving the Helmholtz equation with the boundary element method (BEM). This full-wave solver detects the separate resonance peaks in the scattered field of small bubble ensembles and shows the interaction of many resonances at large

bubble arrays that cover up to a wavelength. These numerical results give new insights into the transition from the downshift in resonance frequency at small bubble ensembles towards the upshift in primary resonance frequency at infinite periodic arrays.

The computational results with the full-wave solver were feasible because of a custom acceleration technique of the BEM for structured arrays of bubbles, reducing the computational complexity to a linear dependence on the bubble count, regardless of their separation distances. Unlike volumetric full-wave solvers such as the finite element method, the BEM solves a boundary integral equation and does not mesh the space between the bubbles. It only needs a surface grid at the bubbles' boundaries and naturally handles the radiation for an unbounded exterior domain. Furthermore, we exploited the translation invariance of Green's functions to compress the all-to-all interaction between the bubbles into a matrix-free implementation of the BEM. These accelerations allowed fast frequency sweeps and accurate simulations for rectangular arrays with hundreds of bubbles.

The following section presents the equations of motion for the bubble dynamics, including the mass-spring model and the Helmholtz equation. The model analysis of the mass-spring system of large bubble ensembles will be presented in Section 2.1 and the accelerated BEM for acoustic transmission in Section 2.2. Section 3 presents the numerical results of the resonance modes of the mass-spring system and the scattered field of large bubble arrays calculated with the BEM.

2 Formulation

The dynamics of an air bubble immersed in a fluid strongly depend on the frequency of the acoustic wave field. This study considers low-frequency wave fields with $0 < a \ll \lambda$ for a the bubble's radius and λ the wavelength of the incident field. In this case, the bubble exhibits a breathing motion, expanding and contracting uniformly. We use two mathematical models: a mass-spring system of ordinary differential equations and the BEM for the Helmholtz equation. The incident wave field will be a plane wave

$$p_{\text{inc}}(\mathbf{x}, t) = P_{\text{inc}} e^{i(k\mathbf{x} \cdot \mathbf{v}_{\text{inc}} - \omega t)} \quad (1)$$

at location $\mathbf{x} \in \mathbb{R}^3$ and time t , where P_{inc} denotes the amplitude, \mathbf{v}_{inc} the propagation direction, k the wavenumber, ω the angular frequency, and i the imaginary unit.

2.1 Mass-spring model

The mass-spring model assumes the bubble to be a monopole point scatterer [3], which is accurate for the low-frequency fields considered in this study and allows for analytical expressions for resonance characteristics.

2.1.1 Single bubble

The equation of motion for a single bubble located at the global origin is given by

$$m\nu''(t) + b\nu'(t) + \kappa\nu(t) = -P_{\text{inc}}e^{-i\omega t}, \quad (2)$$

which is an ordinary differential equation representing a mass-spring system for ν the unknown bubble's volume differential [37]. Notice that this variable only depends on the time since the bubble is assumed to be a point scatterer with monopole dynamics [38]. Furthermore, $m = \rho/(4\pi a)$ denotes the equivalent mass, ρ the fluid's density, $\kappa = 4.2P_A/(4\pi a^3)$ the bubble's stiffness, P_A the ambient pressure, $b = \kappa a/c$ the damping, and c the speed of sound. Here, the damping parameter b includes radiation damping only but could be extended with other damping mechanisms such as thermal and viscous losses [39]. In any case, damping effects are relatively small for air bubbles immersed in water, that is, $0 < b \ll m\omega$.

Taking a harmonic wave field

$$\nu(t) = \bar{\nu}e^{-i\omega t} \quad (3)$$

solves the mass-spring equation (2) for

$$\bar{\nu} = \frac{-\frac{P_{\text{inc}}}{m\omega^2}}{\frac{\omega_0^2}{\omega} - 1 - i\delta} \quad (4)$$

where $\delta = b/(m\omega)$ denotes a non-dimensional damping parameter and $\omega_0 = \sqrt{\kappa/m}$ the natural frequency. Since damping is relatively small, $0 < \delta \ll 1$ and a sharp peak in bubble amplitude is obtained near ω_0 , which is also known as the Minnaert resonance frequency [1]. The quality factor $Q = \omega_0/(\omega_+ - \omega_-)$ characterizes the width of the resonance peak, where ω_{\pm} are the frequencies at which the pressure amplitude is at half power compared to the resonance peak. Specifically,

$$Q = \frac{\sqrt{1 - \delta^2}}{\sqrt{1 + \delta} - \sqrt{1 - \delta}}, \quad (5)$$

which shows the nonlinear relation between the quality factor and the damping parameter.

2.1.2 Multiple bubbles

Let us consider a configuration with N bubbles of identical mass, damping, stiffness, and radius. Their centers are located at $\mathbf{c}_i \in \mathbb{R}^3$ with separation distances $d_{ij} = |\mathbf{c}_i - \mathbf{c}_j| > 2a$ for $i, j = 1, 2, 3, \dots, N$. The same mass-spring system (2) models the dynamics of each bubble, that is,

$$m\nu_i''(t) + b\nu_i'(t) + \kappa\nu_i(t) = -f_i(t) - \sum_{j \neq i} \rho g_{ij} \nu_j''(t), \quad \text{for } i = 1, 2, 3, \dots, N; \quad (6)$$

where

$$f_i = P_{\text{inc}} e^{i(k\mathbf{c}_i \cdot \mathbf{v}_{\text{inc}} - \omega t)}; \quad (7)$$

$$g_{ij} = \begin{cases} e^{ikd_{ij}} / (4\pi d_{ij}) & \text{for } i \neq j, \\ 0 & \text{for } i = j. \end{cases} \quad (8)$$

The extra sum on the right-hand side comes from the self-consistent approach of adding the field scattered from all other bubbles to the incident wave field [20]. This linear system of coupled ordinary differential equations allows a modal analysis of the bubble dynamics. Here, we define a *mode* as a linear combination of bubble movements

$$\mu(t) = \sum_{i=1}^N a_i \nu_i(t) \quad (9)$$

for coefficients $a_i \in \mathbb{C}$, that satisfy a decoupled differential equation

$$m\mu''(t) + b\mu'(t) + \kappa\mu(t) = - \sum_{i=1}^N a_i f_i(t) - \rho\sigma\mu''(t) \quad (10)$$

for $\sigma \in \mathbb{C}$. Because of the linearity of the differential operators, the modes need to satisfy the condition

$$\sum_{j=1}^N \sum_{i=1}^N a_i g_{ij} \ddot{\nu}_j(t) = \sum_{j=1}^N \sigma a_j \ddot{\nu}_j(t), \quad (11)$$

which is equivalent to the eigenvalue problem

$$G\mathbf{a} = \sigma\mathbf{a} \quad (12)$$

whose elements $(G)_{ij} = g_{ij}$ are Green's functions (8). Green's matrix G is complex-valued and symmetric. It is non-normal except for rare bubble configurations. Hence, eigenvalues can be complex-valued and degenerate, and eigenvectors are not necessarily orthogonal. Solving the differential equation (10) with a harmonic function

$$\mu(t) = \bar{\mu} e^{-i\omega t} \quad (13)$$

yields modes given by

$$\bar{\mu} = \frac{-\frac{\bar{f}}{m\omega^2}}{\frac{\bar{\omega}^2}{\omega} - 1 - i\bar{\delta}} \quad (14)$$

where

$$\tilde{f} = P_{\text{inc}} \sum_{j=1}^N a_j e^{ik\mathbf{c}_j \cdot \mathbf{v}_{\text{inc}}}, \quad (15)$$

$$\tilde{m} = m + \rho\Re(\sigma), \quad (16)$$

$$\tilde{b} = b + \omega\rho\Im(\sigma), \quad (17)$$

$$\tilde{\delta} = \tilde{b}/(\omega\tilde{m}), \quad (18)$$

$$\tilde{\omega} = \sqrt{\kappa/\tilde{m}}, \quad (19)$$

$$\tilde{Q} = \sqrt{1 - \tilde{\delta}^2} / \left(\sqrt{1 + \tilde{\delta}} - \sqrt{1 - \tilde{\delta}} \right). \quad (20)$$

Notice that the modal solution (14) has the same structure as the single-bubble case (4) but with different parameters. Furthermore, not all modes are equally excited by the incident wave field. For example, when all bubbles are in a plane perpendicular to the propagation direction of the incident plane wave, we have $\mathbf{c}_j \cdot \mathbf{v}_{\text{inc}} = 0$. Then, the excitation factor

$$\hat{f} = \frac{1}{\sqrt{N}} \left| \sum_{j=1}^N a_j \right| \quad (21)$$

quantifies the relative amplitude of each mode's excitation in the bubble array. Since all eigenvectors \mathbf{a} are normalized, the value of \hat{f} is between zero and one.

2.1.3 Infinite bubble array

A full modal analysis becomes impracticable for periodic arrays of bubbles since an infinite number of modes are present. In the special case where all bubbles are in a plane perpendicular to the excitation direction, one can assume that all bubbles oscillate with identical amplitude at the fundamental mode [40]. This is equivalent to considering a constant eigenvector for the infinite Green's matrix (12). By construction,

$$\sigma_\infty = \sum_j G_{ij} = \sum_{j \neq i} \frac{e^{ikd_{ij}}}{4\pi d_{ij}} \quad (22)$$

for an arbitrary 'center' bubble i . This result is consistent with mass-spring theory for periodic arrays [31], and limits of the infinite series are known for cases such as chains and rectangular array [41].

2.2 Acoustic wave propagation model

The Helmholtz equation accurately models harmonic acoustic wave propagation and, different from the mass-spring approach, includes the bubbles' actual shape. On the downside, solving the system of partial differential equations with numerical methods such as finite differences, finite elements, or the BEM is computationally expensive for large-scale configurations [42].

2.2.1 Helmholtz equation

Let us denote the volume of each bubble by $\Omega_j \subset \mathbb{R}^3$ and its surface by Γ_j for $j = 1, 2, 3, \dots, N$. The boundaries Γ_j have a normal vector $\hat{\mathbf{n}}_j$ of unit length and pointing outward of bubble j . The bubbles are disjoint so that $\Omega_i \cap \Omega_j = \emptyset$, $\forall i \neq j$. Furthermore, we define the variables $\Omega = \bigcup_{j=1}^N \Omega_j$ and $\Gamma = \bigcup_{j=1}^N \Gamma_j$ as the union of the volumes and surfaces, and $\Omega_0 = \Omega^c$ as the unbounded exterior region. The Helmholtz system can then be written as

$$\begin{cases} -\Delta p_{\text{tot}} - k_q^2 p_{\text{tot}} = 0, & \text{in } \Omega_q, \text{ for } q = 0, 1, 2, \dots, N; \\ \gamma_{\text{D},j}^+ p_{\text{tot}} = \gamma_{\text{D},j}^- p_{\text{tot}}, & \text{at } \Gamma_j, \text{ for } j = 1, 2, \dots, N; \\ \frac{1}{\rho_0} \gamma_{\text{N},j}^+ p_{\text{tot}} = \frac{1}{\rho_j} \gamma_{\text{N},j}^- p_{\text{tot}}, & \text{at } \Gamma_j, \text{ for } j = 1, 2, \dots, N; \\ \lim_{\mathbf{r} \rightarrow \infty} |\mathbf{r}| (\partial_{|\mathbf{r}|} p_{\text{sca}} - \imath k_0 p_{\text{sca}}) = 0; \end{cases} \quad (23)$$

where p_{tot} denotes the acoustic pressure, p_{sca} the scattered field and k_i and ρ_i the wavenumber and the density in region i , respectively. The second and third equations are interface conditions for the continuity of the pressure field and normal particle velocity, respectively. The fourth equation is Sommerfeld's radiation condition, modeling the radiation damping of the bubble dynamics. Furthermore,

$$\begin{cases} \gamma_{\text{D},j}^- f(\mathbf{x}) = \lim_{\Omega_j \ni \mathbf{y} \rightarrow \mathbf{x}} f(\mathbf{y}), \\ \gamma_{\text{D},j}^+ f(\mathbf{x}) = \lim_{\Omega_0 \ni \mathbf{y} \rightarrow \mathbf{x}} f(\mathbf{y}), \\ \gamma_{\text{N},j}^- f(\mathbf{x}) = \lim_{\Omega_j \ni \mathbf{y} \rightarrow \mathbf{x}} \nabla f(\mathbf{y}) \cdot \hat{\mathbf{n}}_j(\mathbf{x}), \\ \gamma_{\text{N},j}^+ f(\mathbf{x}) = \lim_{\Omega_0 \ni \mathbf{y} \rightarrow \mathbf{x}} \nabla f(\mathbf{y}) \cdot \hat{\mathbf{n}}_j(\mathbf{x}), \end{cases} \quad (24)$$

with $\mathbf{x} \in \Gamma_j$. The operators $\gamma_{*,j}^\pm$ refer to the traces from the exterior or interior of bubble j , and $\gamma_{\text{D},j}^\pm$ and $\gamma_{\text{N},j}^\pm$ are called the Dirichlet and Neumann traces, respectively.

2.2.2 Acoustic boundary integral equations

Since the bubbles and the exterior domain each have constant density and speed of sound, the scattered field can be represented as

$$p_{\text{sca}} = \sum_{j=1}^N (\mathcal{V}_{0,j} \psi_j - \mathcal{K}_{0,j} \phi_j) \quad \text{in } \Omega_0 \quad (25)$$

where $\phi_j = \gamma_{D,j}^+ p_{\text{tot}} = \gamma_{D,j}^- p_{\text{tot}}$ and $\psi_j = \gamma_{N,j}^+ p_{\text{tot}} = \frac{\rho_0}{\rho_j} \gamma_{N,j}^- p_{\text{tot}}$ are the unknown Dirichlet and Neumann potentials at the surface of bubble j , respectively. Here,

$$[\mathcal{V}_{q,j}\psi](\mathbf{x}) = \iint_{\Gamma_j} G_q(\mathbf{x}, \mathbf{y}) \psi(\mathbf{y}) \, d\mathbf{y} \quad \text{for } \mathbf{x} \in \Omega_q, \quad (26)$$

$$[\mathcal{K}_{q,j}\phi](\mathbf{x}) = \iint_{\Gamma_j} \frac{\partial G_q(\mathbf{x}, \mathbf{y})}{\partial \hat{\mathbf{n}}_j(\mathbf{y})} \phi(\mathbf{y}) \, d\mathbf{y} \quad \text{for } \mathbf{x} \in \Omega_q, \quad (27)$$

are the single-layer and double-layer potential integral operators, with

$$G_q(\mathbf{x}, \mathbf{y}) = \frac{e^{ik_q|\mathbf{x}-\mathbf{y}|}}{4\pi|\mathbf{x}-\mathbf{y}|} \quad \text{for } \mathbf{x}, \mathbf{y} \in \Omega_q \text{ and } \mathbf{x} \neq \mathbf{y} \quad (28)$$

the Green's function of the Helmholtz equation. Different boundary integral equations can be formulated to recast the Helmholtz equation into a surface potential problem at the bubbles' surfaces. The PMCHWT formulation

$$\hat{A}_i \begin{bmatrix} \phi_i \\ \psi_i \end{bmatrix} + \sum_{j=1}^N A_{0,ij} \begin{bmatrix} \phi_j \\ \psi_j \end{bmatrix} = \begin{bmatrix} \gamma_{D,i}^+ p_{\text{inc}} \\ \gamma_{N,i}^+ p_{\text{inc}} \end{bmatrix} \quad \text{for } i = 1, 2, \dots, N, \quad (29)$$

is one of the most robust and accurate choices [43]. Here,

$$A_{0,ij} = \begin{bmatrix} -K_{0,ij} & V_{0,ij} \\ D_{0,ij} & T_{0,ij} \end{bmatrix} \quad \text{and} \quad \hat{A}_j = \begin{bmatrix} -K_{j,jj} & \frac{\rho_j}{\rho_0} V_{j,jj} \\ \frac{\rho_0}{\rho_j} D_{j,jj} & T_{j,jj} \end{bmatrix}, \quad (30)$$

denote the exterior and interior Calderón operators, respectively, where

$$[V_{q,ij}\psi](\mathbf{x}) = \iint_{\Gamma_j} G_q(\mathbf{x}, \mathbf{y}) \psi(\mathbf{y}) \, d\mathbf{y} \quad \text{for } \mathbf{x} \in \Gamma_i, \quad (31)$$

$$[K_{q,ij}\phi](\mathbf{x}) = \iint_{\Gamma_j} \frac{\partial}{\partial \hat{\mathbf{n}}_j(\mathbf{y})} G_q(\mathbf{x}, \mathbf{y}) \phi(\mathbf{y}) \, d\mathbf{y} \quad \text{for } \mathbf{x} \in \Gamma_i, \quad (32)$$

$$[T_{q,ij}\psi](\mathbf{x}) = \frac{\partial}{\partial \hat{\mathbf{n}}_i(\mathbf{x})} \iint_{\Gamma_j} G_q(\mathbf{x}, \mathbf{y}) \psi(\mathbf{y}) \, d\mathbf{y} \quad \text{for } \mathbf{x} \in \Gamma_i, \quad (33)$$

$$[D_{q,ij}\phi](\mathbf{x}) = -\frac{\partial}{\partial \hat{\mathbf{n}}_i(\mathbf{x})} \iint_{\Gamma_j} \frac{\partial}{\partial \hat{\mathbf{n}}_j(\mathbf{y})} G_q(\mathbf{x}, \mathbf{y}) \phi(\mathbf{y}) \, d\mathbf{y} \quad \text{for } \mathbf{x} \in \Gamma_i, \quad (34)$$

are called the single-layer, double-layer, adjoint double-layer, and hypersingular boundary integral operators.

2.2.3 Boundary element method

We discretize the boundary integral equations with a Galerkin method [44]. The test and basis functions are piecewise linear (P1) functions on identical triangular surface meshes for each bubble. The discretized PMCHWT formulation (29)

reads

$$\begin{bmatrix} \hat{\mathbf{A}}_1 + \mathbf{A}_{0,11} & \mathbf{A}_{0,12} & \cdots & \mathbf{A}_{0,1N} \\ \mathbf{A}_{0,21} & \hat{\mathbf{A}}_2 + \mathbf{A}_{0,22} & \cdots & \mathbf{A}_{0,2N} \\ \vdots & \vdots & \ddots & \vdots \\ \mathbf{A}_{N0,1} & \mathbf{A}_{0,N2} & \cdots & \hat{\mathbf{A}}_N + \mathbf{A}_{0,NN} \end{bmatrix} \begin{bmatrix} \mathbf{u}_1 \\ \mathbf{u}_2 \\ \vdots \\ \mathbf{u}_N \end{bmatrix} = \begin{bmatrix} \mathbf{f}_1 \\ \mathbf{f}_2 \\ \vdots \\ \mathbf{f}_N \end{bmatrix} \quad (35)$$

where boldface variables denote matrices or vectors for the respective discretized operators. We use the strong form of the boundary integral operators, which is equivalent to mass-matrix preconditioning of the linear system [45]. Notice that all matrix blocks are dense, modeling all-to-all interactions between the mesh elements on the bubbles' surfaces.

2.2.4 Computational acceleration

The dense matrix arithmetic of the BEM has a restrictive computational complexity in terms of calculation time and memory footprint. Accelerators such as fast multiple methods [46] and hierarchical matrix compression [47] effectively improve the computational efficiency for large-scale simulations such as periodic structures [48]. However, these techniques require high implementation effort and optimization of algorithmic details to achieve significant speedups. Furthermore, our simulations use relatively coarse meshes and need accurate calculations of cross-interactions between bubbles at many frequencies near the Minnaert resonance. For these reasons, we will not use these approaches but instead design a custom acceleration scheme for structured bubble arrays that exploits the translation invariance of Green's functions.

We assume all N bubbles to form a two-dimensional array with constant separation distance. Hence, there are N^2 interactions between the bubbles, including themselves, as modeled by the Calderón blocks (30). Crucially, Green's function is precisely the same when different pairs of bubbles have the same separation distance. Therefore, these Calderón blocks are identical and can be assembled once and reused for all other blocks with the same separation distance. In other words, the number of unique interactions is much smaller than the all-to-all interactions, and the original system (29) can be implemented as a matrix-free algorithm that involves unique Calderón blocks only. More precisely, there are $2(N - 1) + 1$ unique bubble interactions in a rectangular array: one self-interaction and two cross interactions since the direction matters. Every other interaction between bubbles in the array is a duplicate of these.

We can further reduce computation time by considering the symmetry of interactions between pairs of bubbles. Specifically, $\mathbf{V}_{0,ij} = (\mathbf{V}_{0,ji})^T$, $\mathbf{K}_{0,ij} = (\mathbf{T}_{0,ji})^T$, $\mathbf{T}_{0,ij} = (\mathbf{K}_{0,ji})^T$, $\mathbf{D}_{0,ij} = (\mathbf{D}_{0,ji})^T$, and $\mathbf{T}_j = \mathbf{K}_j$; by definition of these operators (31)–(34). Hence, we only assemble the boundary integral operators for $i \leq j$ and transpose them to obtain the operators for $i > j$. Furthermore, the self-interactions require the assembly of three out of four operators.

To summarize, the computational complexity of the standard BEM is $\mathcal{O}(N^2)$. At the same time, the custom acceleration techniques reduce the computational

complexity to $\mathcal{O}(N)$ for calculation time and data storage, where N is the total number of bubbles in the rectangular array. Notice that this is independent of the bubble separation distance since the BEM does not mesh the space between bubbles.

3 Results

This section presents numerical results from computational experiments about collective bubble resonances performed with the mass-spring model and the BEM for the Helmholtz equation. We analyze the behavior of separate modes at increasingly large bubble arrays in Section 3.2 and the acoustic field at resonance frequencies in Section 3.3.

3.1 Parameter settings

All simulations use a speed of sound of 1480 m/s and density of 997 kg/m³ in water, speed of sound of 343 m/s and density of 1.225 kg/m³ in air, and ambient pressure $P_A = 1.01 \cdot 10^5$ Pa. The bubble radius and incident pressure amplitude are normalized to $a = 1$ and $P_{\text{inc}} = 1$, respectively.

The BEM implementation uses the open-source Python library `bempp-cl` [49], with multithreading performed through the `PyOpenCL` library. The mesh width is a third of the bubble’s radius. The iterative GMRES algorithm solves the linear system, without restart and a relative termination criterion of 10^{-5} . The computational simulations were performed on a 12-core Intel(R) Xeon E5-2658A v3, 32 GB RAM machine.

3.2 Modal analysis of collective resonances

The mass-spring model for bubble dynamics presented in Section 2.1 is a system of ordinary differential equations that can be decoupled into independent modes (9). The characteristics of each resonance mode, such as frequency and quality factor, depend on the eigenvalues of Green’s matrix (12). The corresponding eigenvectors determine the excitation factor (21) of each resonance mode. The spectrum, that is, the collection of all eigenvalues, of Green’s matrix is interesting in itself [50, 51, 52] and has implications in different applications such as acoustic metamaterials [23], condensed matter physics [4], and quantum mechanics [8]. Hence, Section 3.2.1 shows the spectrum for increasingly large collections of point scatterers. Section 3.2.2 applies these results to collective resonances of air bubbles immersed in water, showing an initial downshift and subsequent upshift in fundamental resonance frequency at large bubble arrays.

3.2.1 Eigenvalues of Green’s matrix

For a pair of bubbles at distance d between their centers, the eigenvalues of the Green’s matrix are given by $\pm e^{ikd}/(4\pi d)$ and the eigenvectors are $[1, \pm 1]$. These are the well-known symmetric and anti-symmetric proximity resonances [22]

and, when visualized for different distances, are intertwined spirals in the complex plane [8]. For three bubbles at distance d in a triangle, the positive eigenvalue $2e^{ikd}/(4\pi d)$ has a constant eigenvector $[1, 1, 1]$, while the negative eigenvalue $-e^{ikd}/(4\pi d)$ is degenerate with eigenspace spanned by the vectors $[1, 0, -1]$ and $[1, -2, 1]$, which is consistent with known superresonances [3, 27]. Green’s matrix generally is non-normal with complex-valued non-orthogonal eigenvectors that do not include the constant vector. One such example is three bubbles located in a line. Furthermore, the eigendecomposition needs to be calculated numerically for any but trivial configurations.

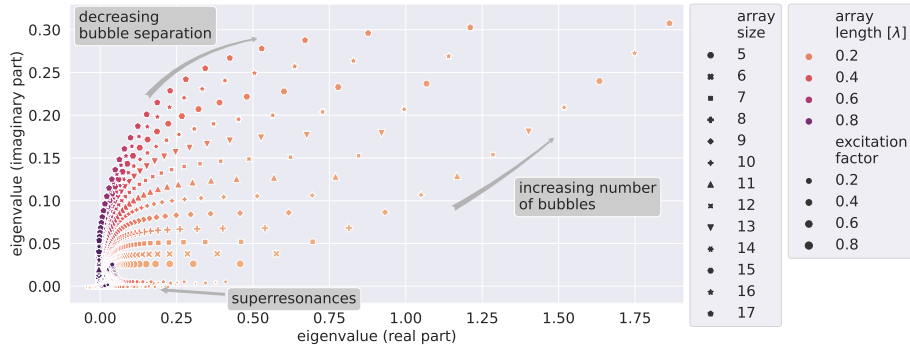


Figure 1: The spectrum of Green’s matrix evaluated at the single-bubble resonance frequency. The rectangular bubble arrays have size $n \times n$, $n = 4, 5, \dots, 17$. The separation distance d increases from two bubble radii with steps of a single radius, while $(n - 1)d < \lambda$. In words, the length of the bubble array does not exceed a wavelength. Only modes with an excitation factor larger than 0.01 are shown.

Figure 1 shows the eigenvalues of Green’s matrix for square bubble arrays with different sizes and separation distances. The results show that in the cases of 1) an increasing number of bubbles at fixed bubble separation and 2) a decreasing bubble separation at fixed bubble count, the eigenvalues grow in both their real and imaginary parts, albeit in different ways. The largest eigenvalue corresponds to the configuration of 17 bubbles located at a distance of two bubble radii, covering less than 10% of a wavelength in total. Furthermore, all eigenvalues with eigenvectors perpendicular to a constant vector were filtered out. The reasoning is that these modes will not be excited by a plane wave. The results show that few superresonances are excited significantly and only at large and densely packed configurations.

Figure 2 shows the eigenvalues of Green’s matrix for a square array of bubbles with constant separation distance and increasingly many bubbles. The results show that configurations extending less than half a wavelength have one dominant mode with an eigenvalue increasing with bubble count. Afterward, the dominant eigenvalue turns around and reaches a limit at a negative real and positive imaginary value. Meanwhile, other modes appear at large array

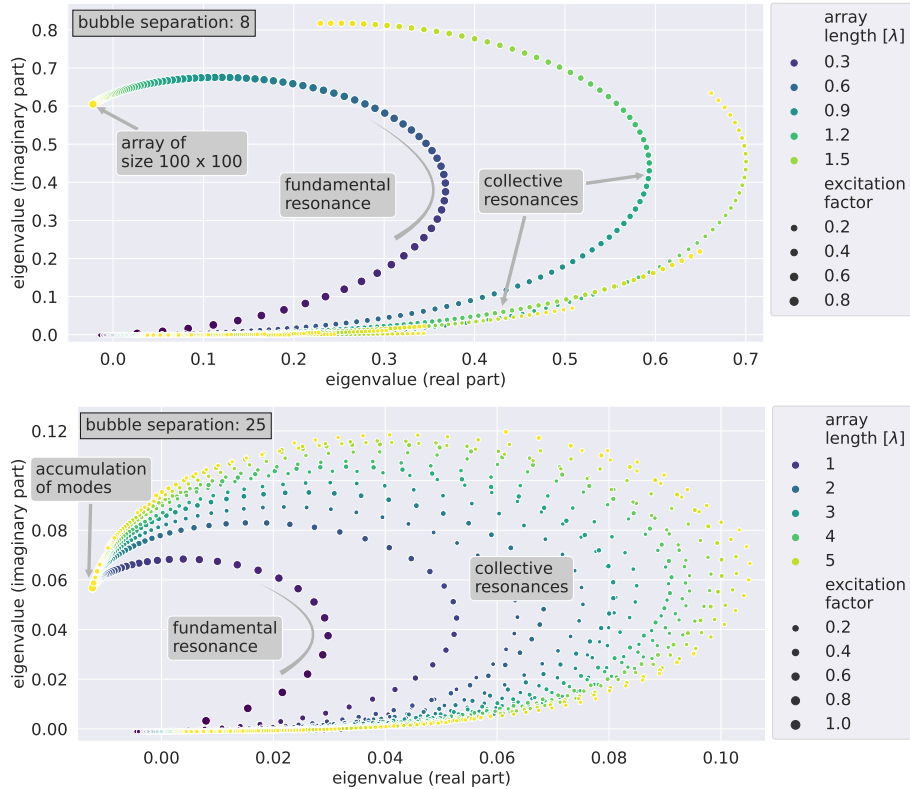


Figure 2: The spectrum of the Green’s matrix evaluated at the single-bubble resonance frequency. The rectangular bubble arrays have size $n \times n$, $n = 2, 5, \dots, 100$ and separation distance of 8 and 25 bubble radii. Only modes with an excitation factor larger than 0.01 are shown.

sizes, with a significant excitation factor and a large eigenvalue. These are interpreted as collective resonances since they only occur when the array covers more than half a wavelength. Those collective modes accumulate at the same value in the complex plane as the fundamental resonance for arrays covering several wavelengths.

3.2.2 Collective resonances in mass-spring systems

The nonlinear relations (19) and (20) calculate each mode’s resonance frequency and quality factor from the eigenvalues of Green’s matrix. Generally, a larger real part of the eigenvalue yields a larger downshift in resonance frequency, and a larger imaginary part yields a broader peak with a smaller quality factor. Hence, the curves in Figure 2 suggest an initial downward and subsequent upward shift in resonance frequency, with an overall widening of the peak for increasingly

large bubble arrays. These results are consistent with the observed downshift in fundamental resonance for small bubble ensembles and an upshift in the dominant mode for infinite periodic arrays, as discussed in the Introduction.

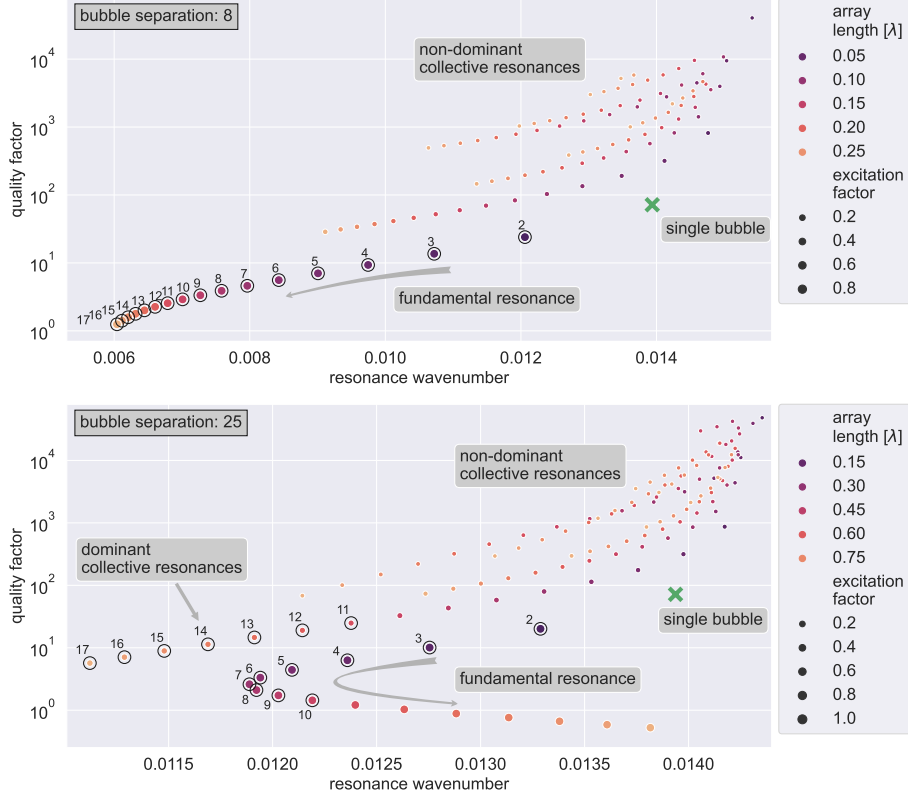


Figure 3: The spectrum of the Green’s matrix evaluated at the single-bubble resonance frequency. The rectangular bubble arrays have size $n \times n$, $n = 2, 5, \dots, 17$ and separation distances of $d = 8a$ and $d = 25a$. Only modes with an excitation factor larger than 0.01 are shown. The numbers highlight the mode with the smallest resonance frequency for the specific array.

Figure 3 shows the resonance wavenumber and quality factor of the modes calculated from the eigenvalues of Green’s matrix. The configurations are square bubble arrays with fixed separation distance and increasing size. The superresonances that are not excited by a perpendicular plane wave were filtered out, and the single bubble was included as a reference. For a short separation distance of eight radii, including more bubbles in the array causes a downshift in frequency and broadening of the fundamental resonance. The collective resonances are never dominant: their excitation factor is small, and their frequency shifts remain limited. Differently, considering a separation distance of 25 radii changes these resonance characteristics. When the bubble array reaches around

half the wavelength, the fundamental resonance displays a return in frequency towards higher values. Moreover, when more than a hundred (10×10) bubbles are present, the second collective resonance mode becomes dominant. It is dominant because it causes the largest downshift in frequency even though it still has a smaller excitation factor than the fundamental resonance mode.

The above presented modal analysis with the mass-spring model shows that the nature of the collective resonances indeed changes when the size of a bubble array reaches half the wavelength. The fundamental resonance remains the mode most strongly excited by a perpendicular plane wave. However, its peak keeps widening while the earlier downshift in frequency changes into an upshift in resonance frequency compared to the single-bubble Minnaert resonance. Furthermore, higher-order collective resonance modes become significant in two ways: they get more strongly excited and display a larger downshift in resonance frequency.

3.3 Acoustic field at collective resonances

The modal analysis gives valuable insights into separate modes of collective oscillations in the bubble array. However, the underlying mass-spring model uses strong assumptions, principally regarding each bubble being a monopole point scatterer. While reasonable at the low frequencies considered here, it has significant limitations in cases such as short separation distances [32, 22]. Furthermore, laboratory experiments measure the acoustic pressure, not separate modes. Alternatively, the Helmholtz equation (23) accurately models the acoustic field scattered by the bubbles. This system of partial differential equations has an analytical solution for single spherically-shaped bubbles [53] and numerical methods efficiently approximate the acoustic field from multiple bubble. The BEM with our custom acceleration algorithm explained in Section 2.2 has linear computational complexity with the number of bubbles in an array and is, therefore, one of the most efficient numerical methods for studying acoustic bubble dynamics. Notice that the BEM solves the Helmholtz equation at multiple frequencies to assess the resonance characteristic for each bubble configuration.

3.3.1 Validation at small arrays

Let us start by comparing BEM's results with the mass-spring model at small bubble ensembles for validation purposes. For an array with four bubbles in a square with separation distance d , the eigenvalues of Green's matrix are $\sigma_0 = 2e^{-ikd}/(4\pi d) + e^{-2ikd}/(8\pi d)$, $\sigma_1 = -2e^{-ikd}/(4\pi d) + e^{-2ikd}/(8\pi d)$, and the degenerate $\sigma_2 = -e^{-2ikd}/(8\pi d)$. The eigenvector of the fundamental mode is constant, while the other eigenvectors represent configurations with neighboring bubbles oscillating in opposite phases. Hence, only the fundamental mode will be excited by a perpendicular plane wave, and its resonance frequency is smaller than for a single bubble. Figure 4 overlays this resonance frequency with BEM's acoustic pressure at a distance of three times a bubble radius away from the array, in the forward direction. Clearly, the peak in acoustic pres-

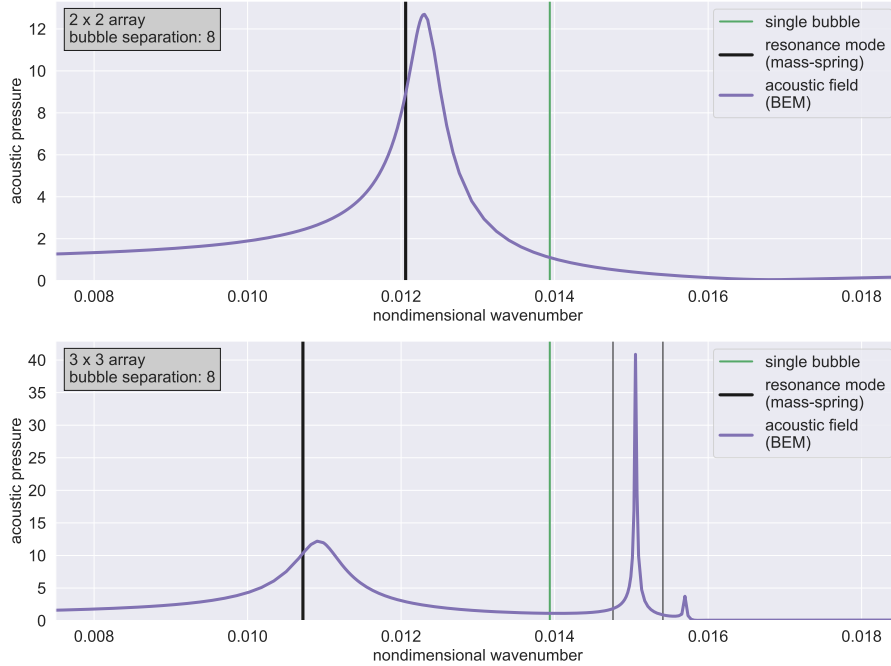


Figure 4: The acoustic pressure calculated at location $(3, 0, 0)$ with the BEM. The incident plane wave field propagates in positive x -direction, and the array is in the (y, z) -plane, centered at the global origin. The vertical lines are the single-bubble Minnaert frequency and the frequency of the collective resonance modes, calculated with the mass-spring model, with the thickness proportional to the excitation factor.

sure corresponds to the expected fundamental resonance at $ka = 0.01206$, lower than for a single bubble. For an array with 3×3 bubbles, the constant vector is not an eigenvector of Green's matrix anymore, and higher-order collective modes will be excited as well, visible by the sharp peaks at higher frequencies than the Minnaert resonance. The expected broadening and downshift of the fundamental resonance with bubble count is also visible in the acoustic field.

3.3.2 Scattering amplitude for large arrays

The incident plane wave excites increasingly many modes of arrays with more bubbles. For example, Figure 5 shows the amplitude of the scattered field at a distance of three bubble radii in the forward direction to arrays with 10×10 bubbles and a separation distance of 8 and 25 radii. In both cases, many sharp collective resonance peaks can be distinguished, some of them with a frequency lower, others with a frequency higher than a single bubble. Notably, the fundamental reference is still visible as a broad peak at the expected frequency

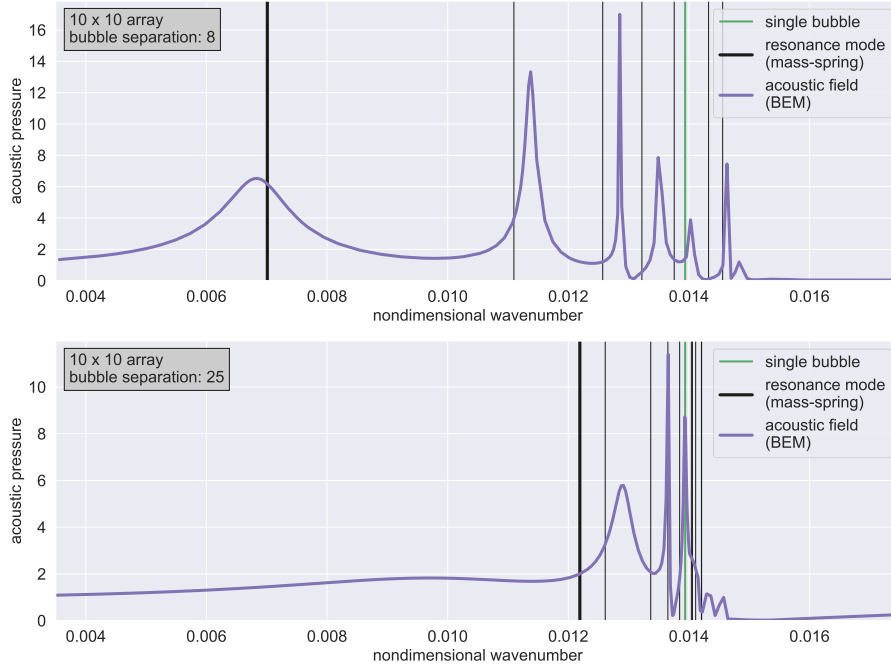


Figure 5: The acoustic pressure calculated at location $(3, 0, 0)$ with the BEM. The incident plane wave field propagates in positive x -direction, and the array is in the (y, z) -plane, centered at the global origin. The vertical lines are the single-bubble Minnaert frequency and the frequency of the collective resonance modes, calculated with the mass-spring model, with the thickness proportional to the excitation factor.

from the modal analysis when the separation distance is 8 radii. Differently, the same array with a separation distance of 25 radii covers more than half the wavelength, and the fundamental and collective resonance cannot be separated anymore from their acoustic responses due to the broad peaks and similar frequencies.

Figure 6 shows the acoustic field scattered from an array of 15×15 bubbles with a separation distance of 25 radii, which covers one wavelength across its diagonal. The fundamental mode is now indistinguishable in the acoustic field. Its frequency is surrounded by collective modes, and its quality factor is so low that its peak amplitude is insignificant.

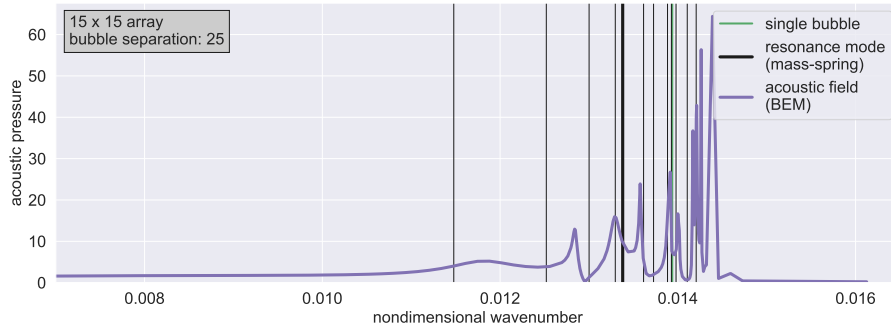


Figure 6: The acoustic pressure calculated at location $(3, 0, 0)$ with the BEM. The incident plane wave field propagates in positive x -direction, and the array is in the (y, z) -plane, centered at the global origin. The vertical lines are the single-bubble Minnaert frequency and the frequency of the collective resonance modes, calculated with the mass-spring model, with the thickness proportional to the excitation factor.

3.3.3 Spatial characteristics of resonance modes

The BEM is a full-wave solver that solves the Helmholtz equation at the surface of each bubble and accurately calculates the acoustic pressure field in the entire three-dimensional space. The following results show the acoustic field scattered from an array of 10×10 bubbles with a separation distance of eight radii at $ka = 0.00678$ and $ka = 0.01136$. These frequencies correspond to the fundamental resonance and the first high-order collective mode, respectively, visible as peaks in Figure 5. All characteristics carry over to a 10×10 array with a separation distance of 25 radii at frequencies $ka = 0.00977$ and $ka = 0.01288$, but these will not be shown here for brevity.

Surface potentials at resonance The solution of the BEM includes surface potentials that represent the acoustic field and its normal derivative at each bubble’s surface. Figure 7 displays the polar decomposition of the complex-valued acoustic pressure at the bubbles’ surfaces. In the fundamental mode, the center bubbles oscillate stronger than the bubbles at the borders because of the multiple interactions between the bubbles. Furthermore, they all oscillate in the same phase, as expected for a monopole resonance. Differently, the center bubbles oscillate in opposite phases to the bubbles at the borders for the collective resonance mode. Moreover, bubbles close to others oscillating in opposite phases have a small magnitude, while bubbles oscillate stronger when surrounded by bubbles with the same phase.

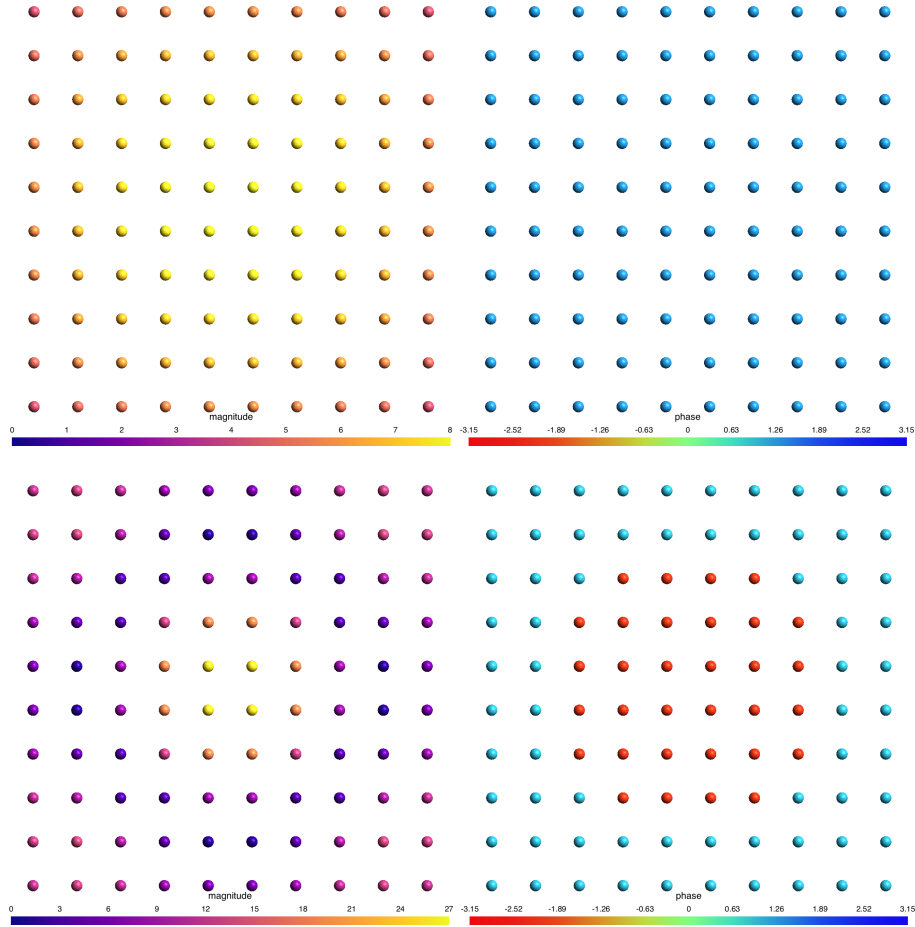


Figure 7: The magnitude (left) and phase (right) of the acoustic pressure at the surface of the bubbles. The array has 10×10 bubbles with a separation distance of eight radii. The normalized wavenumbers $ka = 0.00678$ (top) and $ka = 0.01136$ (bottom) correspond to the fundamental resonance and the first high-order collective mode.

Near field at resonance The oscillations of the bubbles generate an acoustic pressure field in the volume around the array. Figure 8 shows the acoustic pressure amplitude on two slices, one through the array and one perpendicular. At the fundamental resonance, the field is axially symmetric, similar to a monopole field. Differently, the collective resonance displays a shape similar to a multipole field with a large hotspot in the middle and two smaller ones at the far ends. The symmetries in the field are not perfect due to the finite-size effect of the array and distortions from other modes.

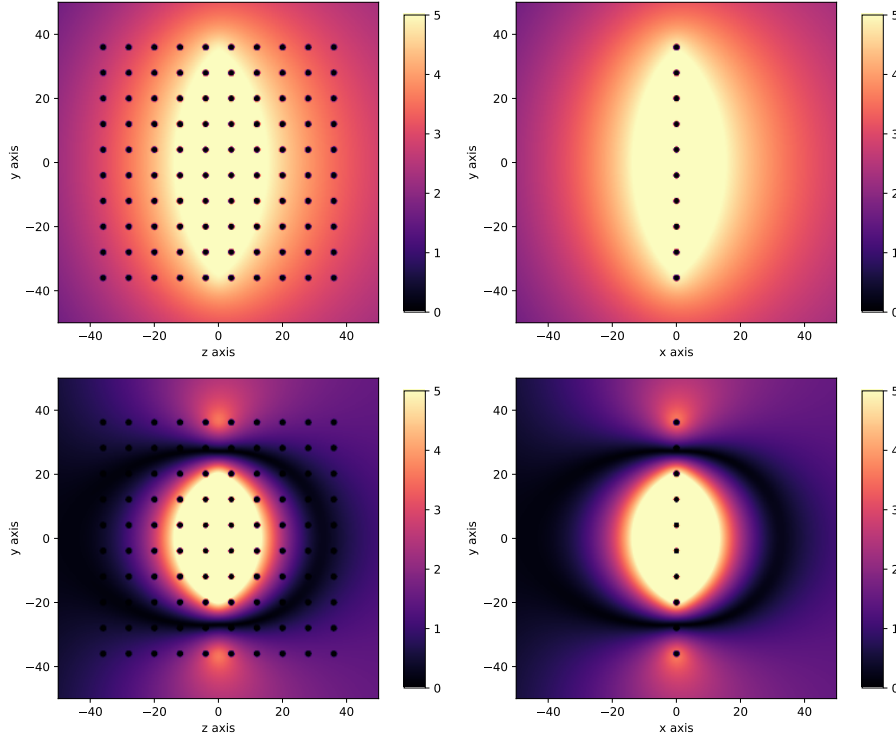


Figure 8: The magnitude of the acoustic pressure at the slices $x = 0$ (left) and $z = 0$ (right). The array has 10×10 bubbles with a separation distance of eight radii. The normalized wavenumbers $ka = 0.00678$ (top) and $ka = 0.01136$ (bottom) correspond to the fundamental resonance and the first high-order collective mode. The axes are normalized by bubble radius.

Far field at resonance The fields from the fundamental and collective resonances are clearly different close to the bubbles, but these differences fade away quickly further from the array. Figure 9 shows the scaled magnitude of the field at a distance of 400 bubble radii. The fundamental resonance has a monopole structure with an axially symmetric field. The collective mode displays a slightly different form, with an elliptic shape in the plane perpendicular to the array, generated by the local hotspots. Furthermore, the far field from the collective mode is smaller, showing how modes other than the fundamental resonance do not tend to radiate far away.

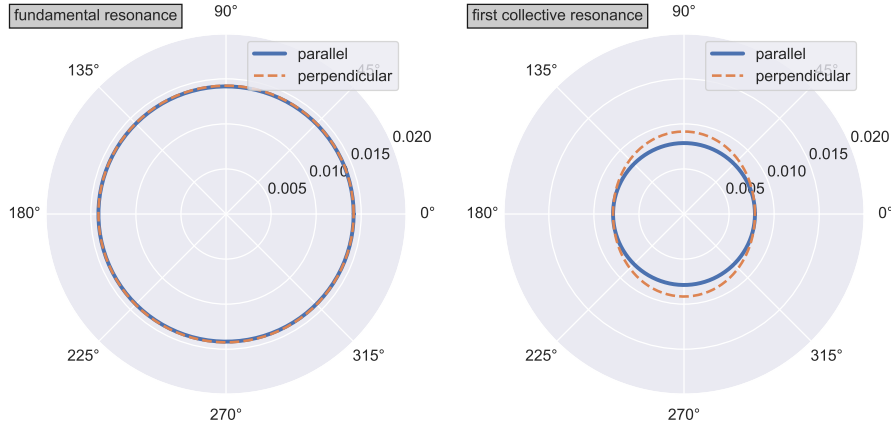


Figure 9: The scaled magnitude of the acoustic pressure, i.e., $R|p_{\text{tot}}|$, on the slices $x = 0$ (parallel) and $z = 0$ (perpendicular) at a distance $R = 400a$ from the global origin. The array has 10×10 bubbles with a separation distance of eight radii. The normalized wavenumbers $ka = 0.00678$ (left) and $ka = 0.01136$ (right) correspond to the fundamental resonance and the first high-order collective mode.

4 Conclusion

The literature on physical experiments and mathematical models regarding the Minnaert resonance shows a downshift in the fundamental resonance of small bubble ensembles and an upshift for large periodic arrays of bubbles. This paper investigated the transition between these situations with a mass-spring model and the full-wave BEM solver. We showed that the modal analysis of the mass-spring model indeed predicts an initial downward shift in resonance frequency for small bubble ensembles, which turns around into an upward frequency motion when more bubbles are present. More precisely, the bubble arrays must cover at least half a wavelength to turn the downward frequency shifts around. At the same time, higher-order collective resonances become significant, being excited stronger by a perpendicular plane wave and having a smaller resonance frequency than the fundamental mode of bubbles oscillating in phase.

We accelerated the full-wave BEM solver and performed high-resolution frequency sweeps over rectangular arrays with hundreds of bubbles. The linear computational complexity of the BEM allowed us to analyze closely-packed bubble arrays that cover half a wavelength. The acoustic field at the surface of the bubbles confirms the almost identical phases of the bubble oscillations at the fundamental modes and bubbles oscillating in opposite phases at the collective modes. These opposite phases generate different hotspots in acoustic pressure inside the array, which are not present at the fundamental frequency. Furthermore, these collective resonances do not radiate as far away as

the axially-symmetric field from the fundamental mode. Concluding, the numerical simulations with the accurate full-wave BEM solver confirm that bubble arrays covering more than half a wavelength have high-order collective modes dominating the fundamental resonance, turning around the downward frequency shifts. Future research targets improving the computational efficiency of the BEM even more so that we can model structures of several wavelengths and investigate the resonance behavior of massive bubble arrays.

References

- [1] Marcel Minnaert. On musical air-bubbles and the sounds of running water. *The London, Edinburgh, and Dublin Philosophical Magazine and Journal of Science*, 16(104):235–248, 1933.
- [2] Victor C Anderson. Sound scattering from a fluid sphere. *The Journal of the Acoustical Society of America*, 22(4):426–431, 1950.
- [3] C Feuillede. Scattering from collective modes of air bubbles in water and the physical mechanism of superresonances. *The Journal of the Acoustical Society of America*, 98(2):1178–1190, 1995.
- [4] Zorana Zeravic, Detlef Lohse, and Wim Van Saarloos. Collective oscillations in bubble clouds. *Journal of Fluid Mechanics*, 680:114, 2011.
- [5] Eric J Heller. Quantum proximity resonances. *Physical Review Letters*, 77(20):4122, 1996.
- [6] M Raveau and C Feuillede. Resonance scattering by fish schools: A comparison of two models. *The Journal of the Acoustical Society of America*, 139(1):163–175, 2016.
- [7] Maxime Lanoy, John H Page, Geoffroy Lerosey, Fabrice Lemoult, Arnaud Tourin, and Valentin Leroy. Acoustic double negativity induced by position correlations within a disordered set of monopolar resonators. *Physical Review B*, 96(22):220201, 2017.
- [8] David Gaspard and Jean-Marc Sparenberg. Resonance distribution in the quantum random Lorentz gas. *Physical Review A*, 105(4):042205, 2022.
- [9] Ali R Kolaini, Ronald A Roy, and David L Gardner. Low-frequency acoustic emissions in fresh and salt water. *The Journal of the Acoustical Society of America*, 96(3):1766–1772, 1994.
- [10] Orest Diachok. Interpretation of the spectra of energy scattered by dispersed anchovies. *The Journal of the Acoustical Society of America*, 110(6):2917–2923, 2001.
- [11] Ira Leifer and Dajun Tang. The acoustic signature of marine seep bubbles. *The Journal of the Acoustical Society of America*, 121(1):EL35–EL40, 2007.

- [12] MR Loewen and WK Melville. A model of the sound generated by breaking waves. *The Journal of the Acoustical Society of America*, 90(4):2075–2080, 1991.
- [13] Helmut Rathgen, Kazuyasu Sugiyama, Claus-Dieter Ohl, Detlef Lohse, and Frieder Mugele. Nanometer-resolved collective micromeniscus oscillations through optical diffraction. *Physical Review Letters*, 99(21):214501, 2007.
- [14] Ben Aldham, Richard Manasseh, Suhith Illesinghe, Kurt Liffman, Andrew Ooi, and Ilija D Šutalo. Measurement of pressure on a surface using bubble acoustic resonances. *Measurement Science and Technology*, 21(2):027002, 2010.
- [15] Chad A Greene and Preston S Wilson. Laboratory investigation of a passive acoustic method for measurement of underwater gas seep ebullition. *The Journal of the Acoustical Society of America*, 131(1):EL61–EL66, 2012.
- [16] Maxime Harazi, Matthieu Rupin, Olivier Stephan, Emmanuel Bossy, and Philippe Marmottant. Acoustics of cubic bubbles: Six coupled oscillators. *Physical Review Letters*, 123(25):254501, 2019.
- [17] Thomas Combriat, Philippine Rouby-Poizat, Alexander A Doinikov, Olivier Stephan, and Philippe Marmottant. Acoustic interaction between 3D-fabricated cubic bubbles. *Soft Matter*, 16(11):2829–2835, 2020.
- [18] Mariem Boughzala, Olivier Stephan, Emmanuel Bossy, Benjamin Dollet, and Philippe Marmottant. Polyhedral bubble vibrations. *Physical Review Letters*, 126(5):054502, 2021.
- [19] Thomas R Hahn. Low frequency sound scattering from spherical assemblages of bubbles using effective medium theory. *The Journal of the Acoustical Society of America*, 122(6):3252–3267, 2007.
- [20] Richard Manasseh and Andrew Ooi. Frequencies of acoustically interacting bubbles. *Bubble Science, Engineering & Technology*, 1(1-2):58–74, 2009.
- [21] Martin Devaud, Thierry Hocquet, Jean-Claude Bacri, and Valentin Leroy. The Minnaert bubble: an acoustic approach. *European Journal of Physics*, 29(6):1263, 2008.
- [22] Elwin van 't Wout and Christopher Feuillade. Proximity resonances of water-entrained air bubbles near acoustically reflecting boundaries. *The Journal of the Acoustical Society of America*, 149(4):2477–2491, 2021.
- [23] V Leroy, M Devaud, T Hocquet, and J-C Bacri. The bubble cloud as an N-degree of freedom harmonic oscillator. *The European Physical Journal E*, 17(2):189–198, 2005.
- [24] Aneta Nikolovska, Richard Manasseh, and Andrew Ooi. On the propagation of acoustic energy in the vicinity of a bubble chain. *Journal of Sound and Vibration*, 306(3-5):507–523, 2007.

- [25] Md Mamunur Roshid and Richard Manasseh. Extraction of bubble size and number data from an acoustically-excited bubble chain. *The Journal of the Acoustical Society of America*, 147(2):921–940, 2020.
- [26] Edward MB Payne, Suhith J Illesinghe, Andrew Ooi, and Richard Manasseh. Symmetric mode resonance of bubbles attached to a rigid boundary. *The Journal of the Acoustical Society of America*, 118(5):2841–2849, 2005.
- [27] Suhith Illesinghe, Andrew Ooi, and Richard Manasseh. Eigenmodal resonances of polydisperse bubble systems on a rigid boundary. *The Journal of the Acoustical Society of America*, 126(6):2929–2938, 2009.
- [28] Maxime Lanoy, Caroline Derec, Arnaud Tourin, and Valentin Leroy. Manipulating bubbles with secondary Bjerknes forces. *Applied Physics Letters*, 107(21):214101, 2015.
- [29] Valentin Leroy, Anatoliy Strybulevych, Maxime Lanoy, Fabrice Lemoult, Arnaud Tourin, and John H Page. Superabsorption of acoustic waves with bubble metascreens. *Physical Review B*, 91(2):020301, 2015.
- [30] Maxime Lanoy, Reine-Marie Guillermic, Anatoliy Strybulevych, and John H Page. Broadband coherent perfect absorption of acoustic waves with bubble metascreens. *Applied Physics Letters*, 113(17):171907, 2018.
- [31] Valentin Leroy, A Strybulevych, MG Scanlon, and JH Page. Transmission of ultrasound through a single layer of bubbles. *The European Physical Journal E*, 29(1):123–130, 2009.
- [32] Valentin Leroy, Nicolas Chastrette, Margaux Thieury, Olivier Lombard, and Arnaud Tourin. Acoustics of bubble arrays: role played by the dipole response of bubbles. *Fluids*, 3(4):95, 2018.
- [33] Gyani Shankar Sharma, Alex Skvortsov, Ian MacGillivray, and Nicole Kessissoglou. Sound scattering by a bubble metasurface. *Physical Review B*, 102(21):214308, 2020.
- [34] David C Calvo, Abel L Thangawng, Christopher N Layman Jr, Riccardo Casalini, and Shadi F Othman. Underwater sound transmission through arrays of disk cavities in a soft elastic medium. *The Journal of the Acoustical Society of America*, 138(4):2537–2547, 2015.
- [35] Maxime Lanoy, Romain Pierrat, Fabrice Lemoult, Mathias Fink, Valentin Leroy, and Arnaud Tourin. Subwavelength focusing in bubbly media using broadband time reversal. *Physical Review B*, 91(22):224202, 2015.
- [36] Valentin Leroy, Alice Bretagne, Mathias Fink, Herve Willaime, Patrick Tabeling, and Arnaud Tourin. Design and characterization of bubble phononic crystals. *Applied Physics Letters*, 95(17):171904, 2009.
- [37] Timothy Leighton. *The acoustic bubble*. Academic Press, New York, 2012.

- [38] Herman Medwin and Clarence S. Clay. *Fundamentals of acoustical oceanography*. Academic Press, New York, 1997.
- [39] Charles Devin Jr. Survey of thermal, radiation, and viscous damping of pulsating air bubbles in water. *The Journal of the Acoustical Society of America*, 31(12):1654–1667, 1959.
- [40] DE Weston. Acoustic interaction effects in arrays of small spheres. *The Journal of the Acoustical Society of America*, 39(2):316–322, 1966.
- [41] Ivan Tolstoy and Alexandra Tolstoy. Line and plane arrays of resonant monopole scatterers. *The Journal of the Acoustical Society of America*, 87(3):1038–1043, 1990.
- [42] Olaf Steinbach. *Numerical approximation methods for elliptic boundary value problems: finite and boundary elements*. Springer, New York, 2008.
- [43] Elwin van ’t Wout, Seyyed R. Haqshenas, Pierre G elat, Timo Betcke, and Nader Saffari. Benchmarking preconditioned boundary integral formulations for acoustics. *International Journal for Numerical Methods in Engineering*, 122(20):5873–5897, 2021.
- [44] Wojciech  migaj, Timo Betcke, Simon Arridge, Joel Phillips, and Martin Schweiger. Solving boundary integral problems with BEM++. *ACM Transactions on Mathematical Software (TOMS)*, 41(2):6, 2015.
- [45] Timo Betcke, Matthew W Scroggs, and Wojciech  migaj. Product algebras for Galerkin discretisations of boundary integral operators and their applications. *ACM Transactions on Mathematical Software (TOMS)*, 46(1):1–22, 2020.
- [46] Nail A Gumerov and Ramani Duraiswami. *Fast multipole methods for the Helmholtz equation in three dimensions*. Elsevier, Amsterdam, 2005.
- [47] Timo Betcke, Elwin van ’t Wout, and Pierre G elat. Computationally efficient boundary element methods for high-frequency Helmholtz problems in unbounded domains. In Domenico Lahaye, Jok Tang, and Kees Vuik, editors, *Modern Solvers for Helmholtz Problems*, Geosystems Mathematics, pages 215–243. Birkh user, Cham, 2017.
- [48] Christopher Jelich, Wenchang Zhao, Haibo Chen, and Steffen Marburg. Fast multipole boundary element method for the acoustic analysis of finite periodic structures. *Computer Methods in Applied Mechanics and Engineering*, 391:114528, 2022.
- [49] Timo Betcke and Matthew W Scroggs. Bempp-cl: A fast Python based just-in-time compiling boundary element library. *Journal of Open Source Software*, 6(59):2879, 2021.

- [50] Marian Rusek, Jan Mostowski, and Arkadiusz Orłowski. Random Green matrices: From proximity resonances to Anderson localization. *Physical Review A*, 61(2):022704, 2000.
- [51] A Goetschy and SE Skipetrov. Non-Hermitian Euclidean random matrix theory. *Physical Review E*, 84(1):011150, 2011.
- [52] SE Skipetrov. Finite-size scaling analysis of localization transition for scalar waves in a three-dimensional ensemble of resonant point scatterers. *Physical Review B*, 94(6):064202, 2016.
- [53] Christopher Feuillade. Superspheroidal modeling of resonance scattering from elongated air bubbles and fish swim bladders. *The Journal of the Acoustical Society of America*, 131(1):146–155, 2012.